# Long-term natural variability and 20th century climate change

Kyle L. Swanson[a,1], George Sugihara[b], and Anastasios A. Tsonis[a]

[a]Atmospheric Sciences Group, Department of Mathematical Sciences, University of Wisconsin, Milwaukee, WI 53201; and [b]Scripps Institution of Oceanography, University of California at San Diego, La Jolla, CA 92093

Communicated by Robert May, University of Oxford, Oxford, United Kingdom, July 31, 2009 (received for review February 20, 2009)

**Global mean temperature at the Earth's surface responds both to externally imposed forcings, such as those arising from anthropogenic greenhouse gases, as well as to natural modes of variability internal to the climate system. Variability associated with these latter processes, generally referred to as natural long-term climate variability, arises primarily from changes in oceanic circulation. Here we present a technique that objectively identifies the component of inter-decadal global mean surface temperature attributable to natural long-term climate variability. Removal of that hidden variability from the actual observed global mean surface temperature record delineates the externally forced climate signal, which is monotonic, accelerating warming during the 20th century.**

climate modeling | ocean variability

Delineating the relative role of anthropogenic forcing, natural forcing, and long-term natural variability in 20th century climate change presents a significant challenge to our understanding of the climate system (1–7). Observations suggest the warming of the 20th century global mean surface temperature has not been monotonic, even when smoothed by a 10–20 year low-pass filter. Temperatures reached a relative maximum around 1940, cooled until the mid 1970s, and have warmed from that point to the present. Radiative forcings due to solar variations, volcanoes, and aerosols have often been invoked as explanations for this non-monotonic variation (4). However, it is possible that long-term natural variability, rooted in changes in the ocean circulation, underlies much of this variability over multiple decades (8–12). Quantifying whether there is a large role for long-term natural variability in the climate system is important, as such variability could exacerbate or ameliorate the impact of climate change in the near future. Further, large magnitude variability may require revisiting the types and magnitudes of imposed forcings thought to be responsible for the observed 20th century climate trajectory (12). More ominously, a climate with large magnitude natural long-term variability in general is a climate very sensitive to imposed forcings, raising concerns about extreme impacts due to future climate change (13).

Due to its large heat capacity, the ocean is the likely source of natural long-term climate variability on interdecadal time scales. The oceans can impact global mean surface temperature in several ways; directly, through surface fluxes of heat, or indirectly, by altering the atmospheric circulation and impacting the distribution of clouds and water vapor. However, our understanding of how the ocean impacts the global mean surface temperature is strongly limited by available observations, which historically have consisted primarily of sea surface temperature (SST) measurements.

The desire to optimally use these SST observations suggests a two-stage approach to objectively quantify the role of internal variability in the 20th century climate trajectory. The first step requires linking SST anomalies to anomalies in the global mean surface temperature. Climate models provide a means to derive such a link, under the assumption that the current generation of climate models captures the essence of the signature of oceanic variability on the global mean temperature. To see that this is the case, we consider annual mean surface temperature fields extracted from 10 multicentury preindustrial control climate simulations, each derived from independently constructed models containing coupled ocean-atmosphere dynamics and advanced physical parameterizations. Such control simulations provide an ideal laboratory for testing ideas about internal variability in the climate because by definition all variability in these simulations is considered to be internal.

From these simulations, we consider the annual mean global mean temperatures and residual anomaly sea surface temperature (RASST) fields (9). Construction of the RASST fields involves first removing the climatology from a given point, as usual for the construction of anomaly fields, and then removing an appropriate global mean value as well. The rationale behind this is that there is no reason why natural long-term variability should be orthogonal to a global warming "mode" that inevitably dominates an empirical orthogonal function decomposition of 20th century fields. The global mean removed here is the mean SST averaged from 60°S to 60°N. Since RASST fields have zero global mean, they have no trivial link to the global mean temperature.

We apply a partition of 30° latitude by 60° longitude to these RASST fields, spanning the 60°S–60°N seasonally ice-free oceanic surface. The average RASST values within these partition elements are used as predictors in a multiple linear regression, with the global mean temperature as the predictand. This procedure is philosophically similar to that used to remove the interannual El Niño signal from observed global mean temperature trends (14), with the caveat that the observed time series are not sufficiently long to statistically identify the signature of inter-decadal internal climate variability on the global mean temperature, necessitating the use of long time-period climate model integrations.

The multiple linear regression provides a series of weights linking the RASSTs within the partition elements to the global mean surface temperature. These weights allow for an objective, statistical prediction of global mean temperature fluctuations arising solely from SST-associated internal variability within a given model. Testing these weights in both preindustrial control and retrospective climate change situations suggests they can successfully identify internal variability (see *SI Text* and Table S1).

**Significantly, the models appear to be consistent in their predicted global mean surface temperature response to RASST anomalies. Fig. 1*A* shows the various models' weights applied to the observed residual anomaly SSTs derived from the extended reconstruction of global SST based upon COADS data (15). The global mean temperature response to observed RASST anom-**

Author contributions: K.L.S. designed research; K.L.S. performed research; G.S. and A.A.T. contributed new reagents/analytic tools; K.L.S., G.S., and A.A.T. analyzed data; and K.L.S., G.S., and A.A.T. wrote the paper.

The authors declare no conflict of interest.

[1]To whom correspondence should be addressed. E-mail: kswanson@uwm.edu.

This article contains supporting information online at www.pnas.org/cgi/content/full/0908699106/DCSupplemental.



www.pnas.org/cgi/doi/10.1073/pnas.0908699106

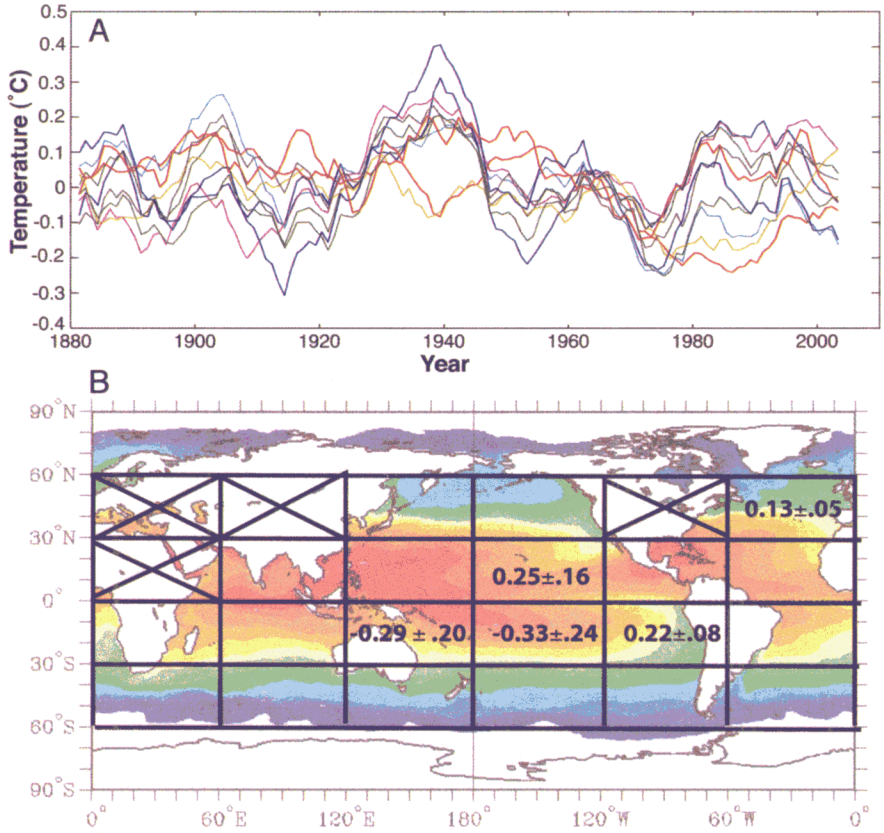


**Fig. 1.** Regression weights derived from preindustrial control climate model simulations allow for estimation of the observed signature of internal variability in the observed 20th century global mean temperature. (*A*) The global mean temperature anomalies resulting from the various models' weights applied to the observed residual anomaly SSTs derived from the extended reconstruction of global SST based upon COADS data (14). The two outlying cold trajectories during the 1940s belong to the GISS-ER and MIROC-MEDRES models. (*B*) The robust weights derived from the preindustrial control simulations. Partition elements where the weights are not significantly different from zero at the $P = 0.1$ level (indicated by the plus/minus) are left blank. Units are °C global mean surface temperature for °C change in SST within the partition element.

alies consistently highlights a cooling from 1900–1915; a warming from 1915–1940; a cooling from 1940 to the late 1970s, and a return to neutral after that point. The exceptions to this behavior are the GISS Model E-R (4.0° × 5.0°) and MIROC 3–2-MEDRES (2.8° × 2.8°), both of which have been documented as having difficulties with air-sea interaction due to limitations in their resolution (16). All other higher resolution models appear to be converging on a common response to observed residual SST anomalies.

Relatively few SST partition elements actively participate in the generation of the global mean temperature fluctuations. Fig. 1*B* shows that over the eight active models, the regression weights differ significantly from zero only in the tropical Pacific and the North Atlantic. Within this context, the spread of the model predicted global mean surface temperatures in Fig. 1a reflects the uncertainty of this technique (90% confidence interval 0.08 °C). Note that this result is not directly a test of model fidelity, but rather of linearity; what is converging here is the model's representations of air-sea interaction leading to global mean surface temperature anomalies, not whether the models have the ability to capture the magnitude or even the spatial patterns of observed RASST variability.

Some caution is necessary in implicating the tropical Pacific and North Atlantic as the primary sources of oceanic-forced variability in the global mean temperature. In particular, multidecadal time-scale variability in the tropical Pacific has global connections (9). As such, variability in the north Pacific, such as the Pacific Decadal Oscillation, that influences the tropical Pacific might well be the ultimate cause of a fraction of observed variability in the global mean temperature. Such concerns, however, are tangential to the global mean temperature signature of oceanic natural variability, which is robust and independent of spatial correlations that might obscure the identification of the precise geographical source of such variability.

While the convergence of the model response to SST variability is encouraging, any technique used to identify internal variability must not be confounded by forced patterns of climate variability. Volcanism, solar forcing, and sulfate aerosols all have a unique "fingerprint" of climate variability, and a useful technique must not confuse such fingerprints with internal variability. Linear discriminant analysis, an exploratory data analysis pattern recognition technique, provides a way to distinguish forced from internal RASST variability when applied in an identical fashion to modeled and observed RASST fields (17). This analysis lifts components of slow interdecadal SST variations from faster intradecadal variations, effectively peeling back layers of longer-time scale variability. These linear discriminants, which consist of an RASST anomaly field and a time series that describes the projection of that anomaly in the annual mean RASST field, maximize the ratio of inter-decadal to inter-annual variability, in keeping with our desire to understand the decadal-to-century scale variability in the global mean surface temperatures (see *SI Text* and Figs. S3 and S4).

**Prior results suggest the leading linear discriminant RASST contains the bulk of the anthropogenic forced climate signal (a mixture of greenhouse gas and aerosols) (17). If our technique**

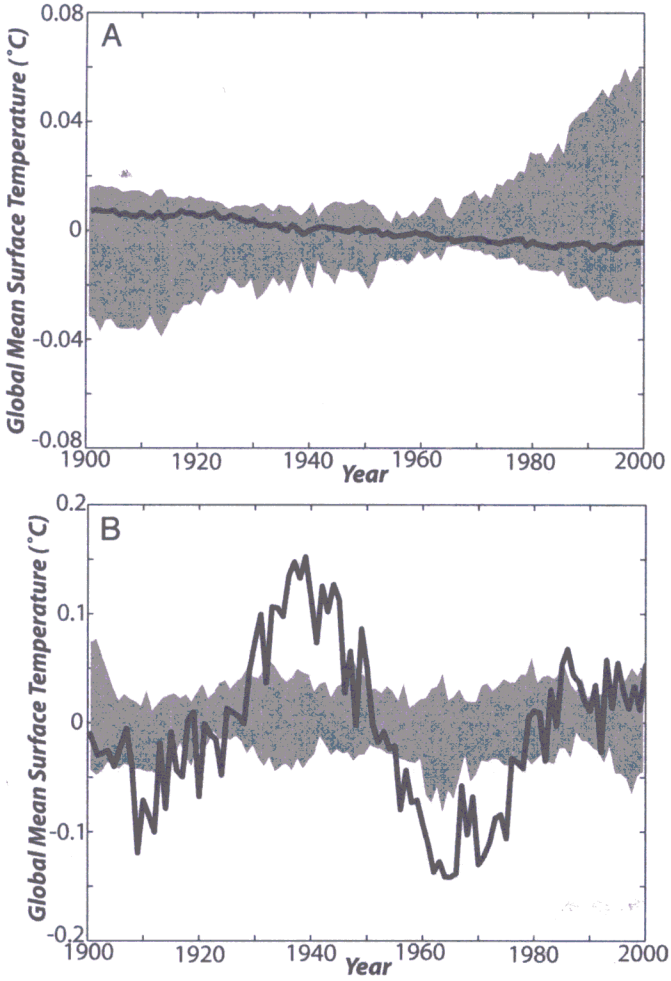


**Fig. 2.** Global mean surface temperature calculated by applying the weights of Fig. 1*B* to the linear discriminants that maximize the ratio interdecadal-to-interannual variability in the residual anomaly SST. The shaded area denotes the 10–90% confidence intervals from the CMIP3 20th century retrospective model ensemble, and the heavy solid curve denotes the global mean temperature signature derived from the discriminant RASST fields. (*A*) Global mean surface temperature associated with the leading discriminant, which contains the forced climate change signal ("footprint"), showing that the weights of Fig. 1*B* are not confounded by this forced pattern in either models or observations. (*B*) Global mean surface temperature associated with higher order oscillatory discriminants. The model mean is indistinguishable from zero throughout the 20th century, suggesting that the observed higher SST discriminants describe internal variability. The underestimation of modeled versus observed interdecadal variability is apparent.

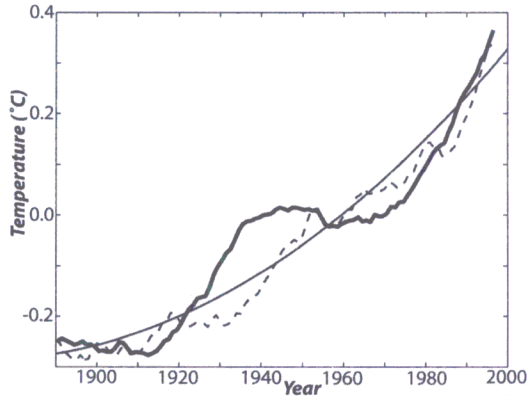


**Fig. 3.** Observed GISS 21-year running mean global mean surface temperature (heavy solid), along with that temperature cleaned of the internal signal, which is the mean over the eight active models of Fig. 1 *A* (dashed). The cleaned global mean temperature warms monotonically, and closely resembles a quadratic fit to the observed 20th century global mean temperature (thin solid). The standard deviation of the cleaned temperature from the quadratic fit is 0.03 °C compared with 0.06 °C for the observed.

is confounded by this signal, there should be a substantial trend in the inferred global mean temperature over the 20th century in both the models and observations, matching the trend in this signal. The shaded area in Fig. 2*A* shows the 10–90% confidence intervals for the global temperature signal associated with the leading linear discriminant in an ensemble of 32 20th century retrospective simulations (20c3m) taken from the CMIP3 archive. No significant trends are found, as the model mean is indistinguishable from zero, with contamination providing at most a warming of 0.1 °C (−0.04 °C to 0.06 °C) over the 20th century. This is not only significantly smaller than the observed 20th century temperature increase of 0.7 °C, but does not have the oscillatory pattern of the temperature anomalies in Fig. 1*A*. Hence, the weights used to define internal variability appear more-or-less blind to this leading pattern of forced RASST variability. The solid curve in Fig. 2*A* shows that the same is true for the leading linear discriminant of observed RASST. Global temperature excursions inferred from this discriminant using the weights of Fig. 1*B* are indistinguishable from zero.

It is possible that oscillatory interdecadal patterns of RASST might be forced as well, perhaps representing some lagged feedback process in the models and in observations. If our technique is confounded by a lagged feedback of some sort, there should be substantial departures of the mean model inferred global temperature from zero, indicating the presence of a forced signal. The shaded area in Fig. 2*B* shows the 10–90% confidence intervals for the global temperature signal associated with higher order, oscillatory discriminants taken from the same ensemble of climate simulations as above. The model mean is indistinguishable from zero for the entire 20th century. Hence, at least in the models, these higher order discriminants describe internal RASST variability.

The lack of a forced SST-associated oscillatory signal in models suggests global temperature anomalies inferred from higher order observed RASST discriminants should signify internal variability. The heavy line in Fig. 2*B* shows the global temperature anomaly associated with these observed oscillatory discriminants consists of an interdecadal global mean temperature fluctuation effectively identical to that in Fig. 1*A*. This oscillatory signal is inconsistent with the model-estimated envelope, as models appear to underestimate inter-decadal variability by a factor of roughly three compared to the observations. This suggests that the current generation of models has difficulty reproducing important aspects of the observed spatiotemporal character of inter-decadal variability (18).

The lack of an oscillatory model signal suggests that the interdecadal global mean surface temperature signal derived from the observations and shown in Figs. 1*A* and 2*B* is indeed the signature of natural long-term climate variability. Removing this internal signature from the observed global mean temperature record should clean up the individual and unique realization of nature, isolating the forced climate signal. Fig. 3 shows that the resulting cleaned signal presents a nearly monotonic warming of the global mean surface temperature throughout the 20th century, and closely resembles a quadratic fit to the actual 20th century global mean temperature. Interdecadal 20th century temperature deviations, such as the accelerated observed 1910–1940 warming that has been attributed to an unverifiable increase in solar irradiance (4, 7, 19, 20), appear to instead be due to natural variability. The same is true for the observed mid-40s to mid-70s cooling, previously attributed

to enhanced sulfate aerosol activity (4, 6, 7, 12). Finally, a fraction of the post-1970s warming also appears to be attributable to natural variability. The monotonic increase of the cleaned global temperature throughout the 20th century suggests increasing greenhouse gas forcing more-or-less consistently dominating sulfate aerosol forcing, although our technique cannot exclude other mechanisms not contained in the current generation of model forcing (22).

This result is another link in a growing chain of evidence that internal climate variability played leading order role in the trajectory of 20th century global mean surface temperature. Freely evolving general circulation model trajectories have been shown to have large global mean surface temperature excursions similar to that observed in the early 20th century (8). These excursions appear to be consistent with fluctuations in the Atlantic thermohaline circulation (THC), which significantly impacts the northern hemisphere temperature (10, 11, 23). The apparent internal variability of the THC has been shown to have a different relation of the SST to subsurface ocean temperatures from that expected for forced variability in the North Atlantic (24), consistent with the THC at least playing a partial role in the internal variability identified here.

A vigorous spectrum of interdecadal internal variability presents numerous challenges to our current understanding of the climate. First, it suggests that climate models in general still have difficulty reproducing the magnitude and spatiotemporal patterns of internal variability necessary to capture the observed character of the 20th century climate trajectory. Presumably, this is due primarily to deficiencies in ocean dynamics. Moving toward higher resolution, eddy resolving oceanic models should help reduce this deficiency. Second, theoretical arguments suggest that a more variable climate is a more sensitive climate to imposed forcings (13). Viewed in this light, the lack of modeled compared to observed interdecadal variability (Fig. 2*B*) may indicate that current models underestimate climate sensitivity. Finally, the presence of vigorous climate variability presents significant challenges to near-term climate prediction (25, 26), leaving open the possibility of steady or even declining global mean surface temperatures over the next several decades that could present a significant empirical obstacle to the implementation of policies directed at reducing greenhouse gas emissions (27). However, global warming could likewise suddenly and without any ostensive cause accelerate due to internal variability. To paraphrase C. S. Lewis, the climate system appears wild, and may continue to hold many surprises if pressed.

**ACKNOWLEDGMENTS.** We thank Isaac Held and Lord Robert May for helpful comments on earlier versions of the manuscript. This work was supported by a grant from the U.S. National Science Foundation under the CLIVAR program (to K.L.S. and A.A.T.). We thank the Lawrence Livermore National Laboratory (http://www-pcmdi.llnl.gov) for the use of their PCMDI archive of climate model data, and the GISTEMP global mean temperature record (http://data.giss.nasa.gov/gistemp).

1. Hegerl GC, et al. (1996) Detecting greenhouse gas induced climate change with an optimal fingerprint method. *J Clim* 9:2281–2306.
2. Barnett TP, et al. (1999) Detection and attribution of recent climate change. *Bull Am Met Soc* 80:2631–2659.
3. Allen MR, Stott PA (2003) Estimating signal amplitudes in optimal fingerprinting, Part I: Theory. *Clim Dyn* 21:477–491.
4. Stott PA, et al. (2000) External control of 20th century temperature by natural and anthropogenic forcings. *Science* 290:2133–2137.
5. Broccoli AJ, et al. (2003) Twentieth-century temperature and precipitation trends in ensemble climate simulations, including natural and anthropogenic forcing. *J Geophys Res* 108:4798.
6. Meehl GA, et al. (2004) Combination of natural and anthropogenic forcings in twentieth-century climate. *J Climate* 17:3721–3727.
7. Stott PA, et al. (2006) Transient climate simulations with the HadGEM1 climate model: Causes of past warming and future climate change. *J Clim* 19:2763–2782 .
8. Delworth TL, Knutson TR (2000) Simulation of early 20th century global warming. *Science* 287:2246–2240.
9. Zhang Y, Wallace JM, Battisti DS (1997) ENSO-like interdecadal variability: 1900–93. *J Clim* 10:1004–1029.
10. Zhang R, Delworth TL, Held IM (2007) Can the Atlantic Ocean drive the observed multidecadal variability in Northern Hemisphere mean temperature? *Geophys Res Lett* 34:L02709.
11. Knight JR, Allan RJ, Folland CK, Vellinga M, Mann ME (2005) A signature of persistent natural thermohaline circulation cycles in observed climate. *Geophys Res Lett* 32:L20708.
12. Hansen J, et al. (2005) Earth's energy imbalance: Confirmation and implications. *Science* 308:1431–1435.
13. Von Storch H, Zwiers FW (1999) in *Statistical Analysis in Climate Research* (Cambridge University Press, Cambridge).
14. Thompson DWJ, Kennedy JJ, Wallace JM, Jones PD (2008) A large discontinuity in the mid-twentieth century in observed global-mean surface temperature. *Nature* 453:646–649.
15. Smith TM, Reynolds RW (2004) Improved reconstruction of SST (1854–1997). *J Clim* 17:2466–2477.
16. Maloney ED, Chelton DB (2006) An assessment of the SST influence on surface wind stress in numerical weather prediction and climate models. *J Clim* 19:2743–2762.
17. Schneider T, Held IM (2001) Discriminants of twentieth-century changes in Earth surface temperatures. *J Clim* 14:249–254.
18. DelSole T (2006) Low-frequency variations of surface temperature in observations and simulations. *J Clim* 19:4487–4507.
19. Hoyt DV, Shatten KH (1993) A discussion of plausible solar irradiance variations, 1700–1992. *J Geophys Res* 98:18895–18906.
20. Solanki SK, Fligge M (1998) Solar irradiance since 1874 revisited. *Geophys Res Lett* 25:341–344.
21. Lee TCK, Zwiers FW, Zhang X, Tsao M (2006) Evidence of decadal climate prediction skill resulting from changes in anthropogenic forcing. *J Clim* 19:5305–5318.
22. Meehl GA, Arblaster JM (2009) A lagged warm event-like response to peaks in solar forcing in the Pacific region. *J Climate* 22:3647–3660.
23. Dima M, Lohmann G (2007) A hemispheric mechanism for the Atlantic multidecadal oscillation. *J Clim* 20:2706–2719.
24. Zhang R (2007) Anticorrelated multidecadal variations between surface and subsurface tropical North Atlantic. *Geophys Res Lett* 34:L12713.
25. Smith DM, Cusack S, Colman AW, Folland CK, Harris GR, Murphy JM (2007) Improved surface temperature prediction for the coming decade from a global climate model. *Science* 317:796–799.
26. Kneelyside NS, Latif M, Jungclaus J, Komblueh L, Roekner E (2008) Advancing decadal scale climate prediction in the North Atlantic sector. *Nature* 453:84–88.
27. Swanson KL, Tsonis AA (2009) Has the climate recently shifted? *Geophys Res Lett* 36:L06711.

# Supporting Information

Swanson et al. 10.1073/pnas.0908699106

## SI Text

**Climate Model Evaluation.** The 10 climate models examined in this study are: GFDL CM2.0; GFDL CM2.1, HadCM3, ECHAM5/MPI-OM; GISS E-R; Canadian Climate Center; CSIRO; MIROC-MEDRES; MRI; and NCAR CCSM. A brief overview of their various underlying dynamical bases can be found in (1). Preindustrial control simulations were extracted from all 10 models, and the global mean temperature from these simulations was filtered using a third order polynomial with respect to time to eliminate century-scale climate drift in that quantity. A multiple linear regression was then done using the RASST values for the partition elements shown in Fig. 1 and the global mean surface temperature fluctuations in each model's control simulation. This regression is based upon a partition that consists of a series of boxes, each 30° latitude by 60° longitude, spanning 180°W–180°E, 60°S–60°N. Boxes with less than 25% ocean area are excluded, leaving 20 total boxes in the regression. The 5-year running mean in Fig. 1*A* is designed to filter out El Niño/Southern Oscillation variability, which has a dominant period in the 2–5 year range; no time filtering is done in Fig. 2 *A* and *B*. Note that the structure of the weights for the multiple linear regression is not sensitive to the choice of filtering time scale, consistent with a linear approach. This regression yields the weights used in the analysis of Fig. 1*A*. Cross-model validation of the weights was performed; for the eight "active" models described in the primary text, using another model's weights typically explains roughly 50% of the interdecadal temperature variance. An example of such agreement is shown in Fig. S1, which shows the use of the HadCM3 model-derived weights on the ECHAM5 model simulation and vice versa.

For the forced retrospective simulations, an ensemble of identically forced simulations for each model is extracted from the CMIP3 archive. We then calculate the global mean surface temperature for a specific realization relative to each model's ensemble mean, along with the RASST for that realization. Note that the latter is not calculated relative to the ensemble mean, as we seek to test whether forced RASST anomalies confound our approach. The weights derived from the preindustrial controls are then used to predict global mean temperature fluctuations arising solely from SST-associated internal variability. Fig. S2 shows a particular 20th century forced simulation derived from the ECHAM5 model with a spectacular internal event consisting of a 0.4 °C warming over the period 1940–1960, indicated by the deviation of the simulation's global mean temperature from an ensemble mean over many identically forced 20th century simulations. The technique here, using the uniform robust weights of Fig. 1*B*, along with the forced simulation's RASST fields as predictors, identifies that particular 1940–1960 warming event as internal, but significantly, not the greenhouse gas-forced warming post-1960. Hence, our method captures the essence of internal global mean temperature variability, while correctly excluding variability associated with external forcing. Removing that internal variability cleans up the individual forced climate change simulation so that it more closely represents the signal, which in this idealized context is the mean over many different dynamical realizations of the climate model, all with identical forcing.

As indicated in Table S1, this ability extends to the 20th century retrospective simulations (32) considered here. Examination of these 20th century retrospective simulations suggests that our approach is not easily confounded; in 24 of the 32 individual forced simulations from 10 different models examined, the robust weights of Fig. 1*B* act to clean up the individual global mean temperature trajectories, reducing the variance of a given realization's interdecadal global mean temperature from the respective model's ensemble mean on average by 11% (Table S1, column 3). This compares favorably to an optimal statistical model based upon each individual ensemble itself on a model-by-model basis, calculated using the ensemble's RASSTs but now relative to the ensemble mean, along with global mean temperature along with global mean temperature anomalies relative to the ensemble mean to construct a multiple linear regression analogous to that shown Fig. 1. Calculating the weights in this manner captures the maximum amount of variance a linear approach can explain in this context, as there is no forced SST signal to confound the approach. This optimal approach reduces the interdecadal temperature variance from its unfiltered level in 29/32 realizations, with an average variance reduction of 38% (Table S1, column 4). Insofar as the technique here, with the single set of robust weights shown in Fig. 1*B* captures a reasonable fraction of this maximum reduction in variance, these robust weights of Fig. 1, and hence our technique, appear not to be significantly confounded by forced variability.

A final test of the potential for climate change to confound this technique is to apply the robust weights to each model's own climate change pattern. This is done by calculating the linear trend in the RASSTs over the 20th century in each individual simulation. The final column in Table S1 shows the fraction of the global mean temperature anomaly resulting from applying the robust weights to this trend RASST anomaly taken over a century. In most cases, the fractional anomaly is on the order of a few hundredths, that is, by and large climate change RASST anomalies lie nearly in the null space for the robust weights, just as appears to be the case for the observed RASSTs as described in the primary text. Curiously, many of the predicted fractional anomalies are negative, suggesting that internal processes based upon climate change RASST patterns in a sense act to counter the direct global temperature anomaly forced by increasing greenhouse gases.

**Linear Discriminant Analysis.** Linear discriminant analysis is an approach taken from pattern recognition theory that allows one to identify climate changes that does not hinge on simulations of natural climate variations or estimates of anthropogenic forcing. Observed interdecadal climate variations are decomposed into several discriminants, which are mutually uncorrelated spatio-temporal components with a maximal ratio of interdecadal-to-intradecadal variance. The technique was introduced to the field by Schneider and Held (2) and in the context here provides a purely observational means by which to extract a signal from time-evolving RASST fields. The linear discriminant analysis here is similar to that done by Schneider and Held, with the exception that we define our groups as contiguous 11-year periods, with significant overlap within the groups, spanning the period 1875–2005. The discriminants shown in the Figs. S3 and S4 are not sensitive to this particular definition, however.

Fig. S4*A* shows the RASST pattern associated with the leading discriminant, which should capture the bulk of the anthropogenic climate change signal in that field. This field has the characteristic warming of the southern relative to the northern hemisphere oceans, broadly considered to be the footprint of sulfate aerosols [see (1), chapter 9]. This discriminant has a ratio $R$ of interdecadal to intradecadal variance of roughly 6, similar to the ratio for the leading mode for full surface temperature

fields (2). It is vital to note that no time dependence is imposed upon the evolution of this discriminant; despite this, the top panel of Fig. S3 shows that the time evolution of this pattern over the period 1920–2000 is quite linear ($r^2 = 0.92$), specifically much more so than the global temperature itself ($r^2 = 0.67$).

The two higher discriminants that are active in determining internal global temperature anomalies are shown in the bottom panels of Fig. S4, although following Schneider and Held (2) it may not be meaningful to view these discriminants separately as their variance ratios are not widely separated. Mode 2 ($R = 4$), the second leading discriminant, appears to describe a pattern similar to that of the Atlantic Multidecadal Oscillation (AMO), with largest temperature variability found in the North Atlantic/North Pacific. Mode 3 ($R = 3$), the third leading discriminant, appears to resemble the tripole pattern associated with the inter-decadal variability of El Niño, with relatively small RASST anomalies outside the Pacific. Other, higher order discriminants beyond those described here are not associated with significant global mean temperature anomalies. The global mean temperature time series resulting from applying the robust weights of Fig. 1*B* to the time-evolving patterns for modes 2 and 3 are shown in the bottom panels of Fig. S3; Mode 2 has the appearance of a pulse of warming centered on about 1940, while Mode 3 is more oscillatory over the 20th century. The sum of these two time series is what is shown in Fig. 2*B*, and effectively explains the bulk of the 20th century global mean temperature signal arising from internal climate dynamics as shown in the primary manuscript Fig. 1. What is important here is that there is no obvious anthropogenic forcing explanation for these modes, as both discriminants 2 and 3 appear associated with well-known patterns of internal oceanic variability.

1. Intergovernmental Panel on Climate Change (2007) Climate Change 2007: The Physical Science Basis. Solomon S, et al., eds. (Cambridge University Press, Cambridge, United Kingdom).

2. Schneider T, Held IM (2001) Discriminants of twentieth-century changes in Earth surface temperatures. *J Clim* 14:249–254.

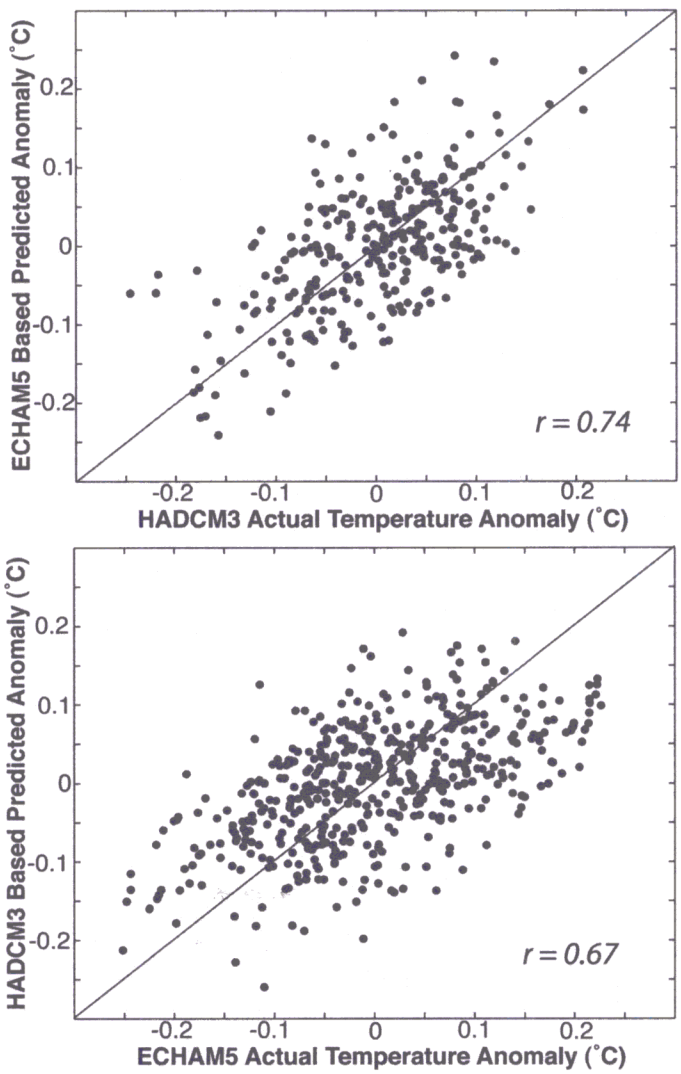


**Fig. S1.** State-of-the-art climate models have the ability to predict each other's global mean temperature anomalies given only information on internal variability. Here we show cross model predicted (ordinate) and actual (abscissa) global mean temperature anomalies using the multiple linear regression technique acting on residual anomaly SSTs from preindustrial simulations, where internal variability is the only source of anomalies in global mean temperature. In each panel the line indicates perfect predictability. The difference in the number of points corresponds to the difference in preindustrial control simulation length – 500 years for the ECHAM5 model and 340 years for the HADCM3.

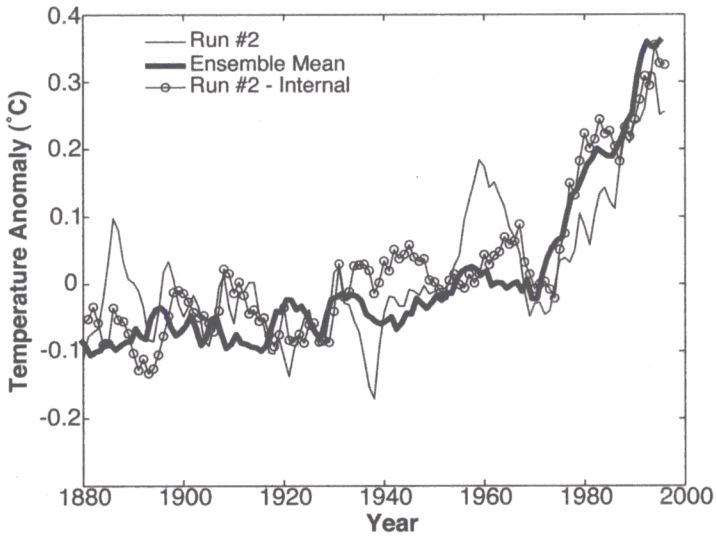


**Fig. S2.** Internally driven global mean temperature anomalies may also be identified in climate models forced by increasing greenhouse gases and other natural and anthropogenic forcings. Here we show global mean temperatures from simulations using the ECHAM5/MPI-OM model that are intended to mimic the climate of the 20th century. Four simulations using identical forcing are examined; the heavy solid curve is the ensemble mean global mean temperature over all four simulations, and the light solid the global mean temperature for run #2. The line with circles is run #2's global mean temperature cleaned of internal climate variability using the multiple linear regression approach outlined here; it is apparent it more closely resembles the ensemble mean, which is the climate signal in this context.

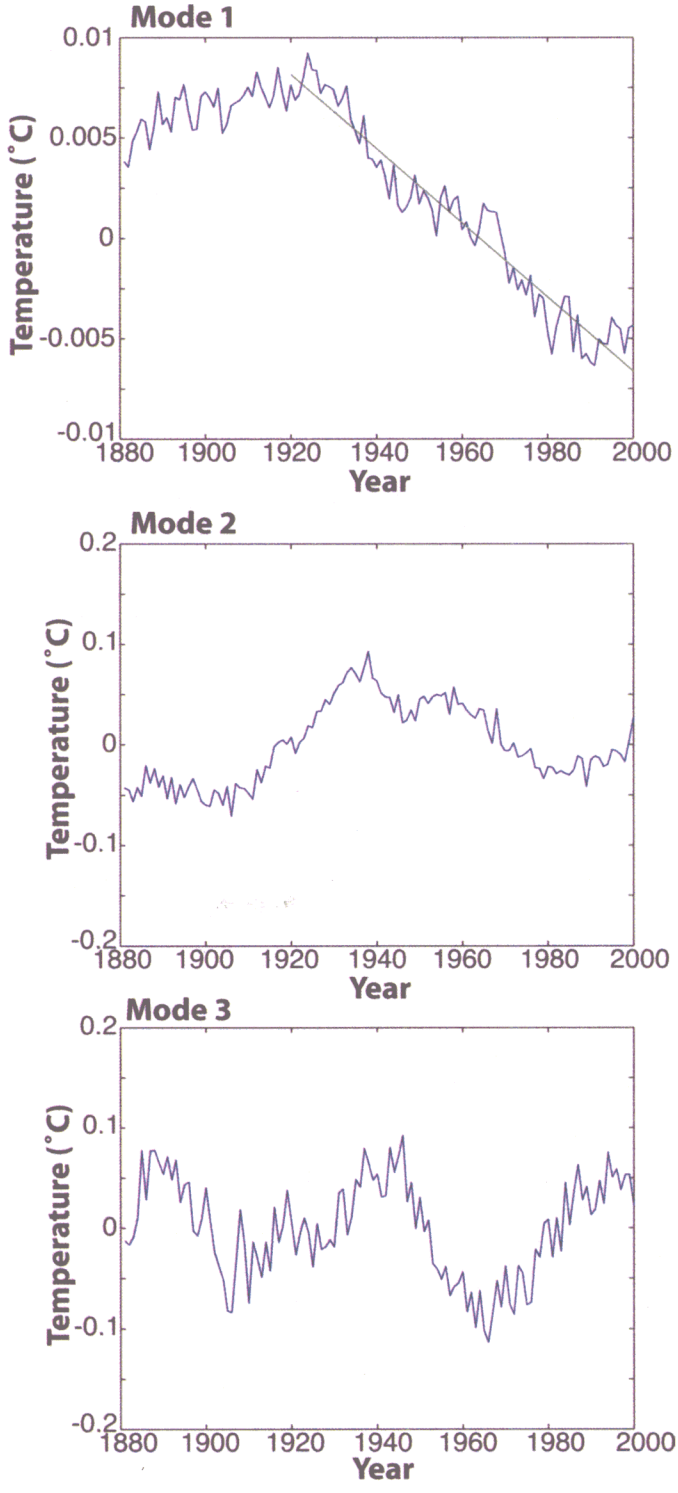


**Fig. S3.** The global mean temperature signatures associated with the 20th century evolution of the leading linear discriminants shown in the primary manuscript's Fig. 2. The leading discriminant is this techniques estimate of the signature of forced climate change, and is very nearly linear over the period 1920–2000. The other discriminants are oscillatory, and their sum yields the global mean temperature perturbation shown in Fig. 2*B*.

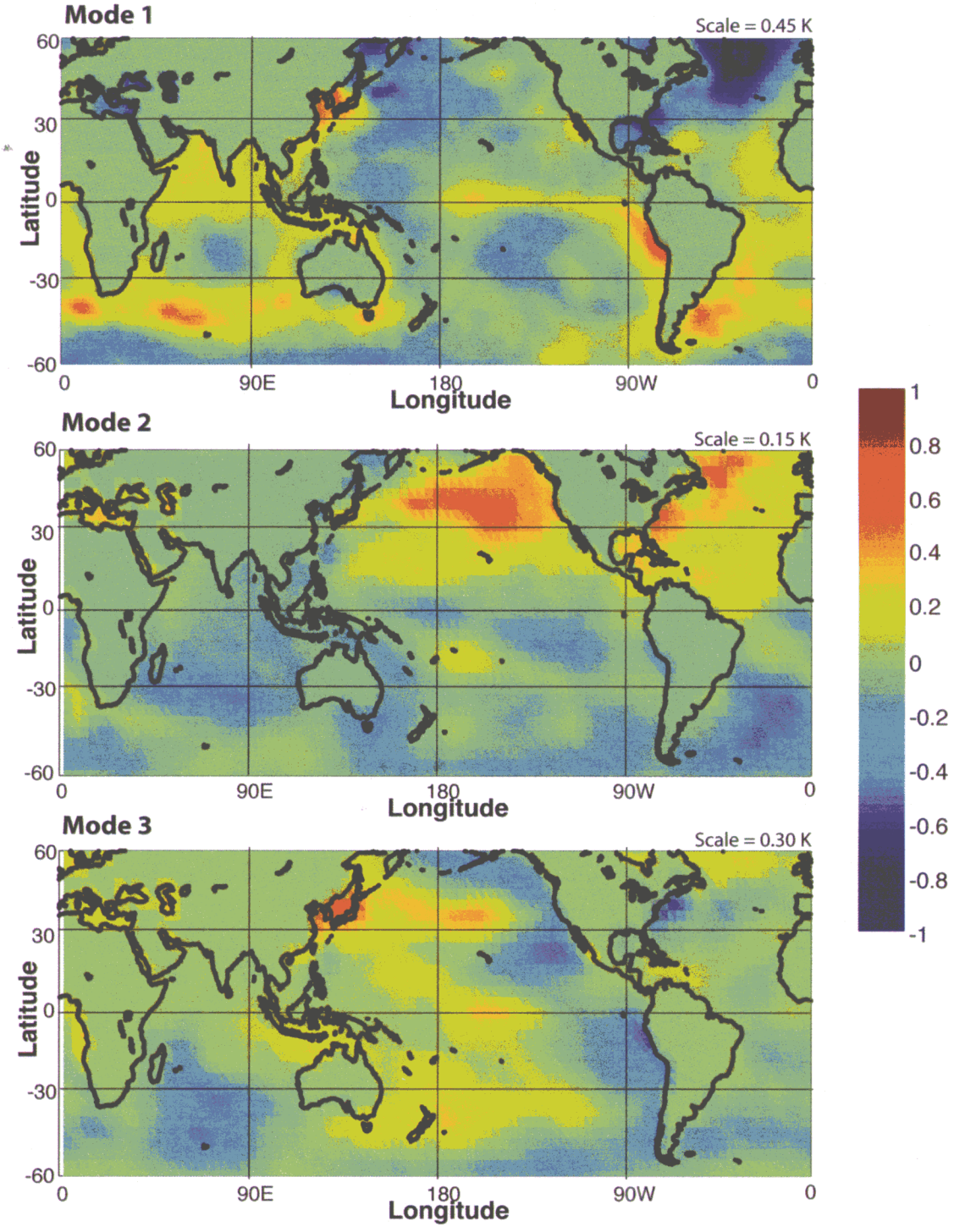


**Fig. S4.** Global sea surface temperature anomalies associated with the leading three discriminants, with the phase consistent with the year 2000. The leading discriminant (Mode 1) has the characteristic cold Northern Hemisphere/warm Southern Hemisphere pattern consistent with preferential cooling of the North due to sulfate aerosol forcing. The second two discriminants have structures reminiscent of the Atlantic Multidecadal Oscillation (Mode 2) and a Pacific tripole consistent with inter-decadal fluctuations in El Niño (Mode 3). The temperature scale is indicated by the color bar, scaled by the temperature anomaly in the upper right hand of each panel.

**Table S1. Standard deviation of decadal-mean global mean surface temperature for thirty-two 20th century retrospective simulations**

| 20c3m Simulations | Decadal STD | Uniform STD | Self STD | Confound |
|---|---|---|---|---|
| GFDL CM2.1 1 | 0.050 | 0.044 | 0.037 | 0.014 |
| GFDL CM2.1 2 | 0.035 | *0.037* | 0.032 | 0.012 |
| GFDL CM2.1 3 | 0.085 | 0.079 | 0.062 | −0.006 |
| GFDL CM2.1 4 | 0.091 | 0.089 | 0.082 | 0.046 |
| ECHAM 1 | 0.043 | 0.037 | 0.032 | 0.001 |
| ECHAM 2 | 0.052 | 0.046 | 0.042 | −0.012 |
| ECHAM 3 | 0.042 | 0.035 | 0.031 | 0.018 |
| ECHAM 4 | 0.055 | 0.045 | 0.042 | 0.018 |
| GISS 1 | 0.030 | *0.031* | 0.021 | 0.018 |
| GISS 2 | 0.019 | 0.018 | 0.012 | 0.051 |
| GISS 3 | 0.029 | *0.033* | 0.024 | 0.025 |
| CCC 1 | 0.030 | 0.029 | 0.027 | 0.025 |
| CCC 2 | 0.024 | *0.025* | 0.022 | −0.016 |
| CCC 3 | 0.037 | 0.034 | 0.028 | −0.001 |
| CCC 4 | 0.023 | 0.022 | *0.026* | 0.011 |
| CSIRO 1 | 0.041 | 0.039 | 0.029 | 0.064 |
| CSIRO 2 | 0.035 | *0.040* | 0.026 | 0.059 |
| CSIRO 3 | 0.060 | 0.051 | 0.045 | 0.059 |
| MIROC MEDRES 1 | 0.039 | 0.033 | 0.031 | 0.031 |
| MIROC MEDRES 2 | 0.027 | 0.024 | *0.031* | 0.031 |
| MIROC MEDRES 3 | 0.039 | 0.033 | 0.028 | 0.005 |
| MRI 1 | 0.026 | *0.031* | *0.041* | −0.009 |
| MRI 2 | 0.041 | 0.035 | 0.034 | −0.028 |
| MRI 3 | 0.045 | 0.039 | 0.028 | 0.016 |
| NCAR CCSM 1 | 0.056 | 0.054 | 0.036 | 0.036 |
| NCAR CCSM 2 | 0.056 | 0.055 | 0.034 | −0.126 |
| NCAR CCSM 3 | 0.061 | 0.047 | 0.051 | −0.01 |
| GFDL CM2.0 1 | 0.096 | *0.099* | 0.065 | −0.052 |
| GFDL CM2.0 2 | 0.085 | 0.072 | 0.059 | −0.045 |
| GFDL CM2.0 3 | 0.060 | *0.063* | 0.052 | −0.024 |
| HADCM3 1 | 0.031 | 0.029 | 0.027 | −0.16 |
| HADCM3 2 | 0.031 | 0.024 | 0.022 | −0.12 |

The column "Decadal STD" refers to the global mean temperature standard deviation from the ensemble mean; "Uniform STD" refers to the global mean temperature "cleaned" of internal variability using the robust weights of Fig. 1*B*; "Self STD" refers to the global mean temperature "cleaned" of internal variability using each model's individual weights calculated from the ensemble itself; and "Confound" measures the fraction of the 20$^{th}$ century global mean temperature change that can be attributed to internal variability, using the robust weights and each realizations RASST patterns.